Thermal Model of the Build Environment for Polyamide Powder Selective Laser Sintering

Timothy T. Diller* Rameshwar Sreenivasan Joseph Beaman David Bourell
Janna LaRocco

Laboratory for Freeform Fabrication
Department of Mechanical Engineering
The University of Texas at Austin
Austin, Texas

Abstract

Precise thermal control of selective laser sintering (SLS) is desirable for improving geometric accuracy, mechanical properties, and surface finish of nylon, or polyamide (PA) parts. A modeling and measurement system was set up to facilitate development of thermal control strategies to improve these characteristics. A SinterStation 2500 SLS machine was used as a test machine for studying builds of parts made of Duraform^{TM} PM nylon powder. Internal temperature measurements of the process were made using resistance temperature detectors (RTDs) embedded in the part bed powder. Surface temperature was measured with an infra-red camera aimed through the front window. A macro-scale time-dependent thermal numerical model of the build chamber and powder bins was developed as a means of evaluating temperature control of the build process. By comparing the measured and predicted temperature profiles, various estimates of the thermal diffusivity of the nylon powder were evaluated.

*Address all correspondence to this author at tdi@mail.utexas.edu.

Background

Build quality of parts made by SLS is determined by several critical criteria, including material strength, surface finish, and dimensional tolerances. These are strongly influenced by the thermal history and geometric details of the part.

Modification of build geometry to accommodate for thermal shrinkage has largely been done based on empirical observation of part deformation after an initial build. Part shrinkage is a function of the thermal gradients in the X-Y plane, that is, in the plane of the build. Manetsberger et al [1] developed a model to predict part shrinkage based on geometry and the thermal environment. Shrinkage in a given build layer is a function of time, temperature, and pressure from the weight of powder above the given layer.

Previous efforts to model thermal aspects of SLS processes with finite-element methods have focused on the small-scale sintering process in the immediate neighborhood of the laser-beam [2–5].

In this work, we broaden the previous work on thermal modeling of SLS processes by taking a macroscopic view of the process and through simulation of the entire thermal environment of the build chamber with the goal of refining the modeled boundary condition at the surface of the part bin.

Material Properties

Several approaches have been used to form an effective thermal conductivity, k_{ef}, for SLS powders [3, 6–8].

Dong *et al* made an estimate based on porosity, ϵ, shown in Eq (1). [3]

$$k_{ef} = k_s \left(1 - C\epsilon\right) \tag{1}$$

where $k_s = 0.28 \left(\frac{W}{mK}\right)$ is the thermal conductivity of the solid material, $C = 1.11$ is an empirical constant and ϵ is defined in terms of the densities of the powder ρ_{powder} and the solid ρ_{solid}:

$$\epsilon = 1 - \frac{\rho_{powder}}{\rho_{solid}} \tag{2}$$

The density of the Duraform PA$^{\text{TM}}$ powder was measured by building a cubic shell and carefully measuring its mass and volume. The cube was emptied and carefully cleaned, and the shell's mass and internal volume were measured again. The density of the powder in the cake surrounding a sintered part was found to be $\rho_{powder} = 490 \left(kg/m^3\right)$. $\rho_{powder} = 1010 \left(kg/m^3\right)$ was used for the density of solid nylon. This yielded a relative part bed porosity of $\epsilon = 49\%$.

Thus, using the porosity method, the estimate of the thermal conductivity of the powder according to Equation (1) was $k_{ef} = 0.17 \left(W/mK\right)$. This method is considered an upper limit on k_{ef} since it assumes a bulk solid with pores and is valid over higher ranges of ϵ that might be found in a sintered part.

The method used by Gusarov *et al* is based on thermal contact between spherical particles but does not account for the conductivity of the interstitial gas [6]. The estimate of k_{ef} is given in Eq (3):

$$k_{ef} = k_s \left(\frac{pn}{\pi}\right) x \tag{3}$$

where p is the relative density, $p = 1 - \epsilon$, n is the coordination number based on the packing configuration, and x is the contact surface ratio, $x = \frac{a}{R}$, where a is the radius of the circular contact region between particles, and R is the particle radius. The relative density for nylon-12 powder in this study was $p = 0.49$ which fell between the calculated relative densities for simple-cubic and diamond packing configurations. The coordination number was estimate by performing a linear interpolation based on the relative densities and coordination numbers of the simple cubic and diamond packing configurations to find $n_{est} = 0.88$.

By this method, k_{ef} is dependent on the contact surface ratio, which was unknown at the time of the study:

$$k_{ef} = 0.88 k_s x \tag{4}$$

This relation is valid for $0 < x < 0.3$, which is given as a reasonable range for non-sintered powders. Thus, a reasonable upper limit on k_{ef} by this method is $k_{ef} = 0.074 \left(\frac{W}{mK}\right)$. The contact surface ratio increases during heating as the powder particles deform and begin to sinter, so that the conductivity may be much lower at the beginning of the build than it is at the end.

Other, more detailed models [7–10] include the effects of interstitial gas and require less empirical fitting but require much more detailed physical characterization of the particles, such as particle surface roughness and deformation properties. At the time of publication, the necessary data for commercial PA powders for SLS was not available in the literature.

A reasonable lower limit for k_{ef} is the thermal conductivity of the interstitial gas: $k_{N_2} = 0.033 \left(W/mK\right)$. The specific heat of $c = 1800 \left(\frac{J}{kgK}\right)$ was assumed to be the same for powder and solid nylon.

In recent work by Dong *et al* [3], the heat flux at the part bin powder surface was modeled as a porous solid as in Eq (5):

$$-k_e \left.\frac{\partial T}{\partial z}\right|_{surf} = h \left(T_a - T_{surf}\right) + \epsilon_R \sigma \left(T_{surf}^4 - T_\infty^4\right) \tag{5}$$

with the convective coefficient assumed to be $h = 25 \frac{W}{m^2 K}$.

Method

Equipment

The machine used for building and modeling in this research was a SinterStation 2500 built by 3D Systems. The build chamber of the machine consists of three powder bins: two feed bins and a part bin, where laser sintering occurs. A movable divider contains a radiant heater over each of the bins for powder heating. During machine operation, the divider is lowered so that the heaters are positioned 9 in (0.23 m) above the powder bed surface. The divider can be raised to facilitate part removal. The center of the heater over the part bin is cut out to allow the sintering laser to shine through to the part bed surface. The interior of the build chamber, with the divider in the lowered position, is shown in Figure 1.

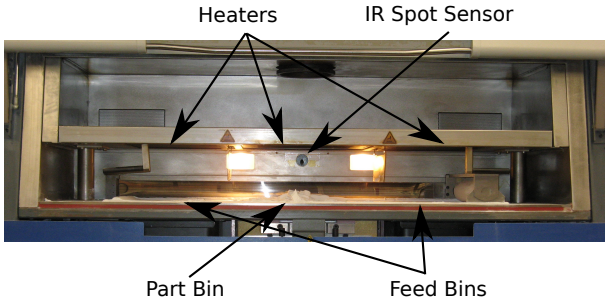

Figure 1: Front view of the build chamber of the SinterStation 2500. Overall interior dimensions are 1.68m by 0.46m (66 in by 18 in).

A build begins when nylon powder is loaded into the bins. The part bin is filled with a thin layer of powder, typically less than 0.5 in, to insulate the top of the part piston. The build chamber is preheated to 80 °C, measured at the powder surfaces, and held for a time to allow the walls to approach thermal equilibrium. After the preheat period, several layers of powder are deposited and heated to 187 °C. Then the sintering begins, with a CO_2 laser beam melting a pattern into the preheated powder. After the pattern has been sintered into each layer, a new layer of powder .004 in (0.1 mm) thick is deposited and preheated. In this way, the part is built up. After the last layer has been sintered, several layers of powder are deposited to insulate the top of the part.

Numerical Model

Overview

In this paper, a 2-D representation of the build chamber of the SLS machine was modeled. The primary goal was to determine the convective and radiative heat fluxes at the powder surface of the part bin. In addition, temperature measurements at the powder surface and in the powder bed were used to tune the simulated heater control. Finally, the 2-D model guided determination of estimates of thermal conductivity of the power based on the different approaches presented earlier.

Software

The geometry for the 2D model was defined and meshed in ANSYS GAMBIT v2.4 using file definitions for Fluent5/6. The numerical simulations were run using ANSYS Fluent v12.1 at the High Performance Computing Laboratory in the Department of Mechanical Engineering at The University of Texas at Austin.

2D Convection Model

The primary goal of developing a two-dimensional model was to understand the magnitudes of convective and radiative heat transfer in the build chamber of the SS2500 in order to accurately specify the boundary condition for the top surface of the build bin.

The geometry for the model was based on a front view of the build chamber and is shown in Figure 2.

The build chamber was purged with heated N_2 at a low replacement rate. The radiant heaters were modeled as heat flux sources on the lower face of the divider structure. Separate boundary faces were set for the feed bin heaters and the part bin heater. Each of the feed bin heaters had a nominal power output of 870 W and had a surface area of $1.187 \times 10^{-1} m^2$, for a total nominal power flux of $7.3 \times 10^3 \frac{W}{m^2}$. The

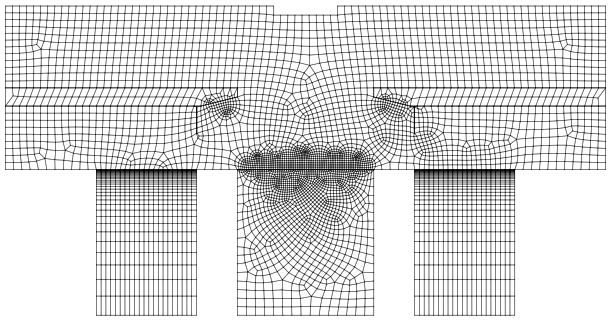

Figure 2: Geometry and mesh for the 2-D model of the SinterStation 2500.

part bin heater had a nominal power output of 1570 W over a surface area of $1.28 \times 10^{-1} m^2$ for a total power flux of $12.27 \times 10^3 \frac{W}{m^2}$.

A software control algorithm in the numerical simulation was set up to mimic the heater controller in the machine, which uses PID control and pulse-width modulation to maintain the surface temperature of the powder bins at a constant $80°C$ for the feed powder bins and $178°C$ for the part bin. In the machine, surface temperature is measured by an IR sensor measuring a spot on the surface of the powder bed. In the simulation, the surface temperature in the middle of the part bed was used to determine the control variable.

By assuming that the power flux Q''_{rad} was dominated by emissive radiation, the surface temperature of each heater could be estimated with the Stefan-Boltzmann law:

$$T = \frac{Q''_{rad}}{\sigma}. \tag{6}$$

with the Stefan-Boltzmann constant $\sigma = 5.67 \times 10^{-8} \frac{W}{m^2 K^4}$. Thus the estimated feed bin heater maximum temperature is $T_{fbheater} = 675K$, and the estimated part bin heater maximum temperature is $T_{pbheater} = 820K$.

The expected temperature range for the nitrogen is approximately 300-500K. Over this range, $N_2$is accurately modeled as an ideal gas with a Prandtl number $Pr = 0.69$ [11]. Because the purge airflow rate is small, movement of the airflow in the build chamber is driven primarily by natural convection at the heater and powder surfaces. The coefficient of thermal expansion, β_{te}, for a gas is given in terms of temperature T, specific volume v, and at contant pressure P by Eq 7

$$\beta_{te} = \frac{1}{v}\left(\frac{\partial v}{\partial T}\right)_P \tag{7}$$

For an ideal gas, β_{te} is given by

$$\beta_{te} = \frac{1}{T}. \tag{8}$$

If the temperature differences are relatively small, that is, if $\beta_{te}\Delta T \ll 1$, then the Boussinesq approximation may be made, in which density is held to be constant except for calculating buoyancy forces. If a mean temperature of $400K$ and a maximum temperature differential of $200K$ are assumed, then $\beta_{te}\Delta T = 0.5$. Thus the Boussinesq approximation should be used with caution. However, in the neighborhood of the powder surface, the temperature differences are expected to be much smaller. If convection is a dominant heat transfer mode in the build chamber, this assumption should be examined more closely.

A surface-to-surface radiation model was used to calculate radiative fluxes in the build chamber. The walls of the build chamber were modeled as 0.0016 m thick steel convective boundaries with convective coefficient $h_{conv} = 0.1\left(\frac{w}{m^2 K}\right)$ and a free stream temperature $T_\infty = 300K$. The walls of the powder bins were modeled as 0.00635 m thick fiberglass convective boundaries with similar h_{conv} and T_∞. The model was run with time steps of 1 second using a density-based solver, and the standard $\kappa - \epsilon$ model for viscosity [12].

Internal Temperature Measurement

Internal measurements were made with RTDs embedded in the build powder. The RTDs were Omega model # RTD-4-F3105-36-T, 100Ω 4-wire units with α-element sensitivity of $0.386\Omega/°C$. The RTDs were mounted on a stand-off attached to the part cylinder piston so that they would remain fixed relative to the part. Because of the very low thermal diffusivity

of the nylon powder, it was critical to minimize the thermal conductivity of the support structure. Thus, a cork standoff was used to support the RTDs.

The RTD signal was recorded every second with a National Instruments *NI 9217* data acquisition system with analog to digital conversion resolution of 24 bits. With the temperature range set to 300-500K, the resolution was $1.2 \times 10^{-2} K$.

Surface Temperature Measurement

Measurements of the temperature at the surface of the part bin were made by means of an infrared (IR) camera. The camera was a FLIR model A325 thermal imaging camera, with a 320X240 pixel resolution and 16-bit resolution. The sensor in the camera measured long-wave $(8 - 12\mu m)$ IR radiation. For the measurements, the camera temperature range was set to 0-500$^\circ C$, yielding a thermal resolution of about 0.03$^\circ C$. Absolute accuracy of the camera was 2 $^\circ C$ for surfaces of known emissivity. Image acquisition rate was adjustable from one-time frame acquisitions (0 Hz) up to 60 times per second. A wide-field lens was fitted to the camera to allow a 90° field of view.

The insulated viewing window on the front of the SLS machine was replaced with an insulated aluminum-and-fiberglass panel with visible- and IR-transparent viewports for the visual inspection and camera viewing, respectively. Because of the geometry of the IR-transparent viewport, some clipping of the image at the inner window occurred. The camera was mounted to the front of the SLS machine and looked through a zinc-selenide window at the part surface as shown in Figure 3. The ZnSe windows had an anti-reflective coating for a transmissivity of greater than 0.98 in the long-wave IR band [13]. The camera was enclosed in a fan-cooled box to protect it from dust and powder in the environment.

The camera was controlled with ResearchIR software from FLIR, which managed both the operating parameters and data acquisition.

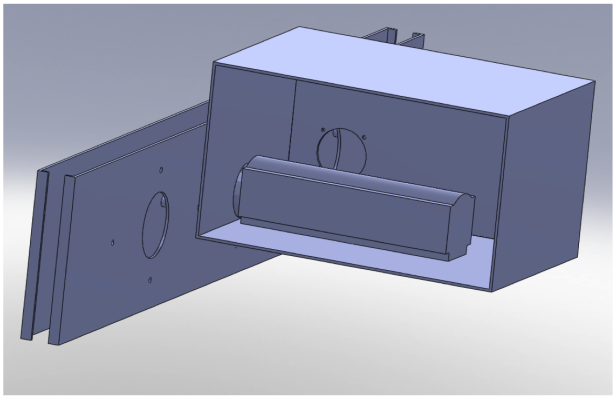

Figure 3: Thermal camera arrangement

Results

Internal Temperatures

The internal temperature measurements were tested during the fabrication of a "sheet of paper". A pair of RTD's was embedded in the part bin, one near the center and one near the right rear corner, 1 inch (25.4 mm) above the piston surface, and $\frac{1}{2}$ inch (13 mm) below the surface. A time history of the RTD signals and depth below the powder surface is plotted in Figure 4.

The machine was preheated to 353K overnight. $\frac{1}{2}$ inch (13 mm) of powder was deposited during the normal warmup cycle, in which the part bed surface was heated to 451K before each successive $\frac{4}{1000}$ inch (0.1 mm) layer of powder was deposited. To heat the first layer during the warmup required about 18 minutes. The remainder of the warmup layers were deposited over the subsequent 68 minutes. One layer of powder was sintered in a 25.7 X 17.2 cm sheet, over 9 minutes. $\frac{1}{2}$ inch (13 mm) of powder was deposited on top of the sintered sheet in $\frac{4}{1000}$ inch (0.1 mm) layers, then the machine was allowed to cool down.

Figure 5 shows the temperatures recorded by RTDs immediately below the surface. Two RTDs were used, placed nominally 0.005" (0.13 mm) below the surface of the powder in the part bin.

In this run, the machine started from ambient temperature (300K) and the heater control was set to

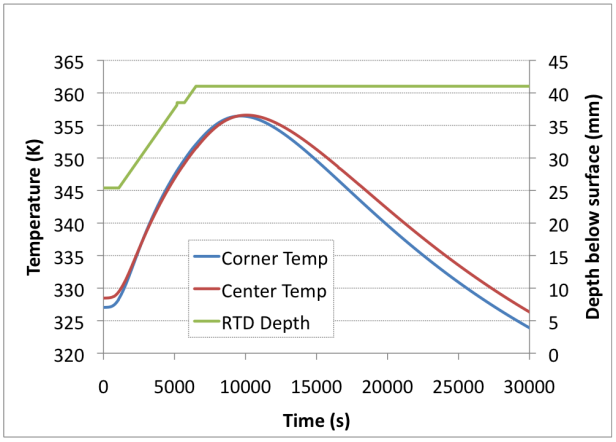

Figure 4: RTD signal during "sheet of paper" build. RTD depth in time is measured on the right-hand scale. RTD temperature is measured on the left-hand scale.

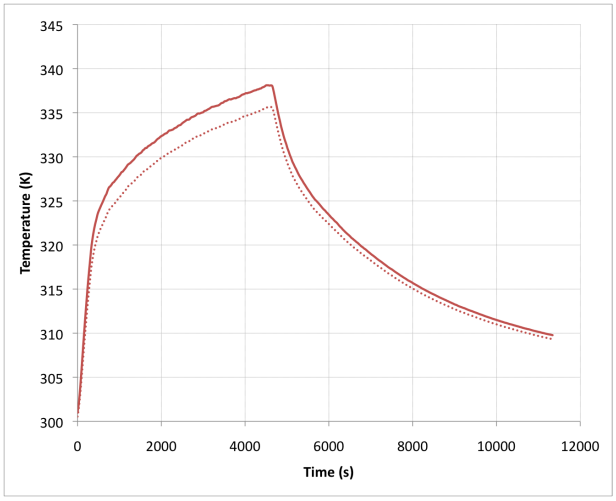

Figure 5: Temperature signal from RTD placed 0.005" below the powder surface of the part bin during a warm-up and cool-down.

373K. The powder surface temperature reached 373K at $t = 900s$, and the heater controller maintained that temperature until $t = 4680s$, when the heater was turned off. Although the two RTD's were placed close together and at the same nominal depth, positioning accuracy was limited, thus the difference between the signals is likely due to differences in depth of placement.

In Figure 6 temperature contours are superimposed on the numerical model grid from Figure 2 at the end of a simulated warmup cycle. The three blue bins at the bottom are the powder bins. The space above the powder bins is N_2 in the range 400-450K. The two hot spots in the center are the radiant heaters, at steady-state at this point in the simulation. The feed bin heaters are not energized because the surface temperature of the feed bins is at or above the set temperature.

The temperature gradient $\frac{dT}{dy}$ at the surface of the powder bin was 4320 $\left(\frac{k}{m}\right)$ in the center; the mean convective heat flux to the surface was -21 $\left(\frac{W}{m^2}\right)$; the mean radiative flux to the powder surface was 248 $\left(\frac{W}{m^2}\right)$, and the mean convective coefficient at the powder surface was 2.4 $\left(\frac{W}{m^2K}\right)$. Thus, the radiative heat flux dominated the convective heat flux at the powder surface by an order of magnitude.

Surface Temperatures

Both the IR camera and the SLS machine's own IR sensor were used to track the part bed surface temperature. A paint of a known emissivity (0.95) was applied in a test pattern to the surface of a sintered nylon sheet. The nylon sheet was attached to a surface at about 100 $°C$. Comparison of the thermal signatures of the exposed sintered nylon and the test pattern in the camera image revealed the emissivity of the nylon surface to be 0.95 in the long-wave infrared band. The surface was found to be diffuse for angles down to about 15° to the surface.

Figure 7 gives a thermograph of the build chamber near the end of warmup period. The scale is clipped in this image so that temperatures over 480K appear as 480K and temperatures below 360K appear as 360K.

The prominent hot-spot in the upper half is the radiant heater. The walls of the mounting tube form a circular mask around the image, clipping the sides of the heater and the near corners of the powder bed

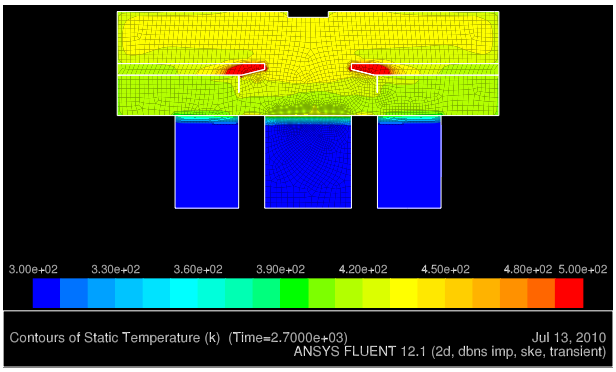

Figure 6: Temperature profile of 2-D numerical model at the end of simulated warmup to 451K.

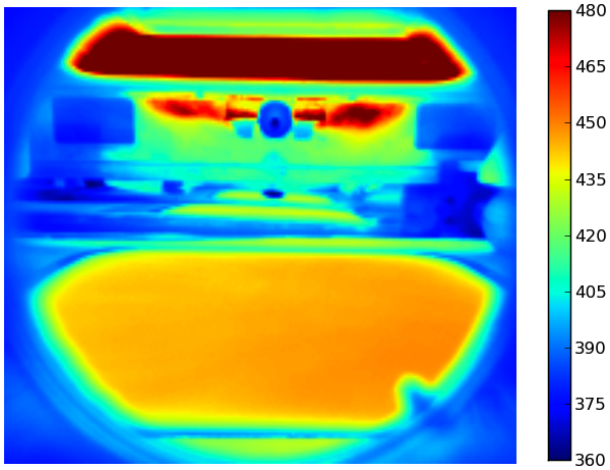

Figure 7: Temperature distribution at part bin surface (Temperatures in K).

surface. Two cooler rectangles at about 3/4 of the image height are the visible-light lamp covers. A cool circle in the middle of the image between the lamp covers appears where the IR sensor for controlling the heaters is located. The hot spots either side of the IR sensor are reflected images of the heater.

The back wall of the build bin is largely reflective, including a flexible stainless steel baffle which seals the opening for the powder roller drive mechanism. Because of the reflectivity of the back wall images of the powder bed surface and the heater are visible in the middle of the image.

The powder bed surface is visible in the lower half of the image. A cool protrusion into the powder bed surface at the lower right is a set screw that holds the ZnSe window in place.

In Figure 8, the thermograph from Figure 7 has been clipped to just the powder bed surface, and the temperature scale has been adjusted to highlight the thermal gradient that exists at the surface. From the back left corner to the front right corner of the powder bed, a difference of approximately 13K exists.

The IR camera was removed from the mounting box and repositioned to point at the surface of the heater over the part bin. The heater was turned on, and a thermograph was made, as shown in Figure 9. As before, the temperature scale is clipped, with a lower limit of 510K and an upper limit of 610K. The upper edge of the image corresponds to the edge of the heater nearest the front of the build chamber, and the bottom to the rear. Right and left match the thermographs of the powder bin surfaces.

A substantial non-uniformity of temperature is evident over the heater surface. A prominent hot spot exists on the right-hand side of the heater, being approximately 30K warmer than the left side.

The SLS machine's own IR sensor measured a spot near the center of the part bed surface. In Figure 10, the IR sensor temperature and the simulated surface temperature in the numerical model are plotted against time during a pre-heat event.

The data from the machine IR sensor is plotted with a solid black line. Three simulation cases are plotted as well, representing the three calculation methods for k_{ef}. The porosity-based method ($k_{ef} = 0.1714\left(\frac{W}{mK}\right)$) is plotted with a red line marked with x's. The Gusarov method ($k_{ef} = 0.0739\left(\frac{W}{mK}\right)$) is plotted with a dashed blue line. The estimated lower limit based on the interstitial gas ($k_{ef} = 0.0326\left(\frac{W}{mK}\right)$) is plotted with a green dotted line. Data acquisition for the IR sensor started after the warmup had already begun so that the starting temperatures are not the same.

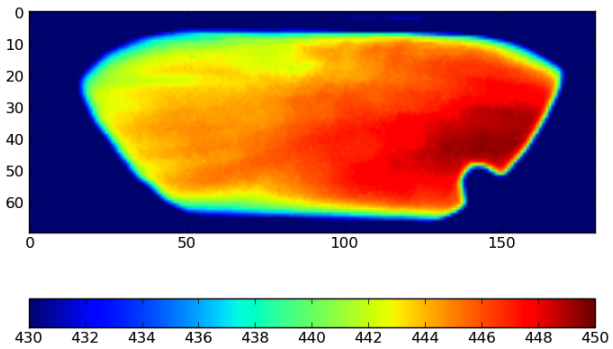

Figure 8: Part bed surface temperature (in K)

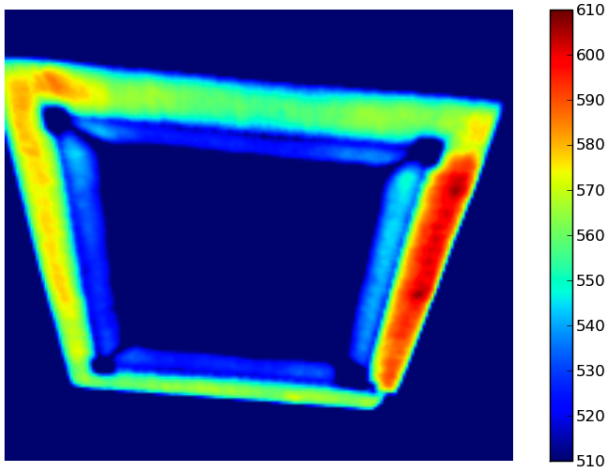

Figure 9: Thermograph of the part bin heater surface. Temperatures are in K.

Discussion & Conclusions

Temperature measurements in the powder cake around the part confirmed the low thermal diffusivity of nylon powder. It is interesting to note, for instance, that in the case reported in Figure 4, the machine had been left to warm up to 352K overnight. Although the interior space was at steady state, the initial temperature recorded by the RTD's was 25K below the surface temperature. The peak temperature reached at the surface during the build was 451K, yet the peak temperature recorded by the RTD was 91K lower. The lower temperatures recorded by the corner RTD are explained by its proximity to the part bin wall.

A similar phenomenon was observed with the more shallowly placed RTD's in Figure 5. Here the maximum surface temperature was 373K, and the peak temperature recorded by an RTD nominally 0.005 in (0.000127 m) below the surface was 337K, a thermal gradient of 280,000 $\frac{K}{m}$. This is substantially higher than the thermal gradient 4300 $\frac{K}{m}$ predicted by the numerical model with the Gusarov estimate of effective thermal conductivity. The likely explanation is that the positioning of the RTD was inexact, and with such a high thermal gradient, any error in RTD placement is strongly magnified.

The presence of the thermal gradient across the surface of the powder was not entirely surprising. Parts positioned in the front right corner of the part bin were immediately below the hot spot, and it was considerably more difficult to remove the powder cake in that area. The temperature distribution at the powder surface had not previously been quantified. The implications for part quality are substantial. That is, monitoring and maintaining the radiant heaters is shown to be important for part quality.

The numerical model was successful in reproducing the general thermal characteristics of the build chamber, although some fine tuning is necessary. In Figure 10, the initial gradient of surface temperature in time is most closely matched by the Gusarov and porosity-based thermal conductivity cases. All of the simulated cases overshot the set temperature, however, indicating that the simulated heater control algorithm did not successfully match the controller in the machine. With further work, this can be improved substantially. Assessment of the various k_{ef} models will rely in future work on carefully placed and controlled RTD measurements.

Nevertheless, certain insights can be gained from the model. First, the powder can support very high thermal gradients over long time periods, leading to long cycle-times during part warmup and cooling. Second, radiation dominates the heat transfer in the build chamber, and convection plays a very minor role. The convective coefficient predicted by the nu-

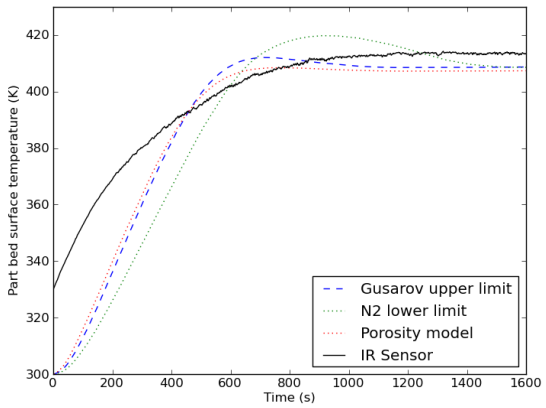

Figure 10: Measured and simulated surface temperatures during a part bed pre-heat from 300K to 413K.

merical model was an order of magnitude lower than that assumed by Dong *et al* [3]. Additionally, this validates the use of the Boussinesq approximation for convection in the build chamber.

In future work, the material property estimates will be refined based on experimental results and further characterization. The simulated heater control algorithm will be refined to more closely approximate the behavior of the machine. Finally, a 3-D model will be developed to model the deposition and sintering of powder.

Acknowledgements

This research was funded by the Department of Defense under grant #GRT00015778.

References

[1] Manetsberger, K., Shen, J., and J., M., 2001. "Compensation of non-linear shrinkage of polymer materials in selective laser sintering". *Solid Freeform Fabrication Proceedings.*

[2] Schultz, J., 2003. "Modeling heat transfer and densification during laser sintering of viscoelastic polymers". PhD thesis, Virginia Tech.

[3] Dong, L., Makradi, A., Ahzi, S., Remond, Y., and Sun, X., 2008. "Simulationof the densificationof semicrystalline polymer powders during the selectivelasersinteringprocess: Application to nylon12". *Polymer Science Series A,* ***50***(6), June, pp. 704–709.

[4] Kandis, M., and Buckley, C., 1999. "An engineering model for laser-induced sintering of polymer powders.". *Journal of Manufacturing Science & Engineering,* ***121***(3), p. 360.

[5] Kandis, M., Buckley, C., and Bergman, T., 1998. "A model of polymer powder sintering induced by laser irradiation". In Heat Transfer 1998, Vol 5 - General Papers, Lee, JS, ed., Korean Soc Mech Engineers, Taylor & Francis, Ltd., pp. 205–210. 11th International Heat Transfer Conference, Kyongju, South Korea, Aug 23-28, 1998.

[6] Gusarov, A. V., Laoui, T., Froyen, L., and Titov, V. I., 2003. "Contact thermal conductivity of a powder bed in selective laser sintering". *International Journal of Heat and Mass Transfer,* ***46***(6), pp. 1103 – 1109.

[7] Slavin, A., Londry, F., and Harrison, J., 2000. "A new model for the effective thermal conductivity of packed beds of solid spheroids: alumina in helium between 100 and 500 c". *International Journal of Heat and Mass Transfer,* ***43***(12), pp. 2059–2073.

[8] Slavin, A., Arcas, V., Greenhalgh, C., Irvine, E., and Marshall, D., 2002. "Theoretical model for the thermal conductivity of a packed bed of solid spheroids in the presence of a static gas, with no adjustable parameters except at low pressure and temperature". *International Journal of Heat and Mass Transfer,* ***45***(20), pp. 4151–4161.

[9] Hall, R., and Martin, D., 1981. "The thermal conductivity of powder beds. a model, some

measurements on uo2 vibro-compacted microspheres, and their correlation". *Journal of Nuclear Materials,* ***101***(1-2), pp. 172 – 183.

[10] Achenbach, E., 1995. "Heat and flow characteristics of packed beds". *Experimental thermal and fluid science,* ***10***(1), pp. 17–27.

[11] Mills, A. F., 1999. *Heat Transfer*, 2^{nd} ed. Prentice Hall, Upper Saddle River, NJ.

[12] ANSYS. *ANSYS FLUENT 12.0/12.1 Documentation.*

[13] ISP Optics, 2010. *BBAR-ZNSE-8-12 Data Sheet.* http://www.ispoptics.com, July.